

Aerodynamic and Acoustic Optimization for Fan Flow Deflection

Andrew D. Johnson¹, Juntao Xiong², Sara Rostamimonjezi³, Feng Liu⁴, and Dimitri Papamoschou⁵
University of California, Irvine, CA 92697, USA

This investigation seeks to optimize the implementation of fan flow deflection for jet noise suppression from a supersonic turbofan nozzle with bypass ratio 2.7. The design objective is to maximize reduction of noise perceived by the community while minimizing aerodynamic losses. An adjoint method for shape optimization is used to obtain deflector vane designs with sufficient flow deflection and minimum thrust penalty. A NACA0012 airfoil is used as the initial shape for the vane airfoil. Optimization leads to reduction in specific-thrust loss and a thicker airfoil which is beneficial for structural reasons. The optimal vane airfoil is used in a parametric acoustic study of 50 deflector configurations with variable vane chord length, angle of attack and azimuth angle. The best configuration leads to reductions in effective perceived noise level (EPNL) of 2.8 dB in the downward direction and 2.5 dB in the sideline direction. Addition of a porous wedge-shaped fan flow deflector increases the EPNL reductions to 5.0 dB and 3.9 dB in the downward and sideline directions, respectively.

Nomenclature

c	=	vane chord length
B	=	boundaries of the computational domain
C_p	=	pressure coefficient
D	=	computational domain
D_f	=	nozzle fan diameter
EPNL	=	effective perceived noise level
f_i	=	inviscid convective flux in the physical domain
f_{vi}	=	viscous convective flux in the physical domain
I	=	cost function
K_{ij}	=	transformation functions between the physical and computational domain
L	=	lift
M	=	Mach number
NPR	=	nozzle pressure ratio
p	=	static pressure
q	=	dynamic pressure
R	=	governing flow equations
s	=	entropy per unit mass
\bar{s}	=	mass-averaged entropy
T	=	thrust
T_s	=	specific thrust
W	=	conservative variable vector
x_i	=	coordinates in the physical domain
α	=	angle of attack
α_W	=	wedge half-angle
ε	=	plume deflection angle

¹ Post Doctoral Researcher, Department of Mechanical and Aerospace Engineering, adjohnso@uci.edu, AIAA Member.

² Post Doctoral Researcher, Department of Mechanical and Aerospace Engineering, jxiong@uci.edu, AIAA Member.

³ Graduate Researcher, Department of Mechanical and Aerospace Engineering, srostami@uci.edu, AIAA Student Member.

⁴ Professor, Department of Mechanical and Aerospace Engineering, fliu@uci.edu, AIAA Associate Fellow.

⁵ Professor, Department of Mechanical and Aerospace Engineering, dpapamos@uci.edu, AIAA Fellow.

ξ_i	=	coordinates in the computational domain
Λ	=	weight of penalty function
Φ	=	observation azimuth angle
ϕ	=	deflector azimuth angle
Ψ	=	co-state variable

I. Introduction

INCREASINGLY stringent regulations for aircraft noise emission during takeoff continues to generate a demand for new and innovative methods for jet noise reduction. A prevailing method for reducing jet noise from both subsonic and supersonic aircraft is through fan flow deflection (FFD).¹ The general approach employs aerodynamic deflectors to direct the fan flow of a separate-flow nozzle downward with respect to the core flow as illustrated in Fig. 1. This reduces velocity gradients and turbulent kinetic energy (TKE) production on the underside of the jet, thereby suppressing noise emission in the downward and sideline directions.² Deflectors have encompassed airfoil-shaped vanes internal to the fan duct² as well as deployable wedge-shaped flaps located outside the fan nozzle.³

Effective use of the FFD method requires careful optimization. As with many noise reduction techniques, there are opposing acoustic trends and aerodynamic performance factors that need to be balanced properly. While the overall trend of downward noise suppression with TKE reduction on the underside of the jet is understood, localized increases of TKE on the upper side of the jet, for large downward fan flow deflections, can generate excess noise. The excess noise can propagate downward and offset the benefit derived from the TKE reduction. It is manifested as a cross-over in the sound pressure level spectra and affects mainly the large polar angles from the jet axis. This suggests that there is an optimal overall deflection angle. The deflectors themselves should be optimized from an aerodynamic standpoint, minimizing entropy generation and avoiding shock phenomena that penalize thrust and can create their own excess noise. The aerodynamic and acoustic optimizations are thus interconnected and should be addressed in a unified fashion.

The first part of the paper addresses the optimization of the deflector vanes. Past experiments utilized vanes with standard airfoil sections (NACA0012, NACA4412 and NACA7514).⁴ These airfoils were designed for constant freestream environments, while the FFD vane airfoils are immersed in an externally-imposed favorable pressure gradient (accelerating freestream) due to the convergence of the fan duct. Computations of the flow field inside the fan nozzle revealed that the symmetric NACA0012 airfoil has a tendency of generating excessive suction near the leading edge, while the cambered NACA4412 and NACA7514 airfoils produce a large supersonic pocket over the airfoil resulting in the formation of a strong shock wave.⁵ These undesirable characteristics of standard airfoil shapes motivated the design for an optimum vane shape for FFD applications, using an adjoint optimization method.

In the second part of the paper, the optimal vane airfoil is used in a parametric acoustic study of 50 deflector configurations with variable vane chord length, angle of attack and azimuth angle. Special nozzles were designed that enabled an efficient and consistent evaluation of these configurations in a subscale environment. The resulting optimal vane configuration is then combined with a wedge-shaped fan flow deflector to achieve very significant reductions in effective perceived noise level.

II. Deflector Optimization

A. Design Methodology

The separate-flow turbofan nozzle considered in this study is based on a scaled down version of the 3BB nozzle used for noise reduction research at the NASA Glenn Research Center. The 3BB nozzle has a nominal bypass ratio of $BPR = 5.0$ with convergent exit streamlines typical to modern turbofan engine nozzles. The variant used here has been scaled down by a factor of eight to ensure compatibility with the flow rate capabilities of the experimental aeroacoustic facility. The fan diameter was further reduced to produce a bypass ratio of $BPR = 2.7$ at the exhaust conditions shown in Table 1, which have been determined via the engine cycle analysis performed in Ref.6. The coordinates of the resulting nozzle (referred to as the B27 Nozzle) are shown in Fig. 2. The Reynolds number based on the fan diameter was 0.92×10^6 .

The vane fan flow deflectors are installed in a single- or dual-pair arrangement inside the fan duct, with the airfoil trailing edge a short distance upstream of the fan exit plane. For a four-vane configuration, the lower and upper vane pairs are mounted symmetrically about the nozzle midplane at azimuthal angles of $\pm\phi_1$ and $\pm\phi_2$, respectively, as illustrated in Fig. 3. In practice, the deflector vanes would likely be actuated so that they can be deflected when noise reduction is desired and otherwise remain at zero angle of attack. For this reason, only

symmetric airfoil-shaped vanes are considered in this study in order to minimize losses when the vanes are in the neutral position.

The objective of the optimization is to achieve a target flow deflection angle while minimizing the aerodynamic losses caused deflector vanes. The aerodynamics losses are quantified in terms of the mass-averaged entropy generation

$$\bar{s} = \frac{\int_{B_e} s \rho \mathbf{u} \bullet \mathbf{n} dA}{\int_{B_e} \rho \mathbf{u} \bullet \mathbf{n} dA} \quad (1)$$

where $\mathbf{u} \bullet \mathbf{n}$ denotes the flux through the fan nozzle exit surface B_e . The flow deflection is quantified in terms of the overall downward turning angle

$$\varepsilon = \frac{1}{T} \int_{B_e} \rho u v dA \quad (2)$$

with the nozzle thrust T obtained by integration of the axial momentum and pressure on the exit surface of the fan nozzle.

$$T = \int_{B_e} (\rho u^2 + p - p_a) dA \quad (3)$$

Accordingly, the cost function is

$$I = \bar{s} + \Lambda |\varepsilon - \varepsilon_0| \quad (4)$$

where ε_0 is the target deflection angle and Λ is the weight of the penalty function. The vane airfoil design parameters are Hicks-Henne shape functions distributed along the upper surface of the vane. The lower surface is identically perturbed to fulfill the requirement of a symmetric section.

B. Adjoint Method

The shape optimization is based on the adjoint approach developed by Jameson⁷ and Jameson et al.⁸ The variation of the cost function consists of a term due to the variation of the flow field and another due to the modification of the boundaries. The variation of the flow field δW implicitly depends on the variation of the geometry δF through the Navier-Stokes equations. By multiplying the variation of the governing flow equations $\delta R(W, F)$ by a Lagrange multiplier Ψ^T and adding it to the variation of the cost function, the explicit dependence of δI on δW can be removed by setting

$$\left[\frac{\partial I}{\partial W} \right]^T - \left[\frac{\partial R}{\partial W} \right]^T \Psi = 0 \quad (5)$$

which is recognized as the adjoint equation. The variation of the cost function then simplifies to

$$\delta I = G \delta F \quad (6)$$

where G is the gradient

$$G = \left[\frac{\partial I}{\partial F} \right] - \Psi^T \left[\frac{\partial R}{\partial F} \right] \quad (7)$$

The optimization problem reduces to solving the governing flow equations and their corresponding adjoint equations to find the value of Ψ . The gradient is easily computed for large numbers of design parameters because the computational cost depends only on the perturbation of the geometry.

In this study, the cost function has been defined as an integral over the fan nozzle exit (Eqs. 1-4). A weak form of the Navier-Stokes equations can be written as

$$\int_D \frac{\partial \Psi^T}{\partial \xi_i} (\delta F_i - \delta F_{vi}) dD - \int_B \Psi^T (\delta F_i - \delta F_{vi}) dB = 0 \quad (8)$$

where the first term is integrated over the computational domain D and the second term is integrated over the domain boundary B . The symbols $F_i = S_{ij} f_j$ and $F_{vi} = S_{ij} f_{vj}$ denote the inviscid and viscous convective fluxes transformed to the computation domain using the coordinate transformation $K_{ij} = \partial x_i / \partial \xi_j$ with $S_{ij} = J K_{ij}^{-1}$ and $J = \det(K)$. Adding Eq. 7 to the variation of cost function, we have

$$\delta I = \int_{B_c} \delta C dB - \int_B n_i \Psi^T (\delta F_i - \delta F_{vi}) dB + \int_D \frac{\partial \Psi^T}{\partial \xi_i} (\delta F_i - \delta F_{vi}) dD \quad (9)$$

where C is a scalar function of both the flow variables and the geometric variables and depends on the definition of the cost function.

The term δC is further divided into the terms δC_f , denoting the flow variation, and δC_g , denoting the geometry variation. δC_f can be used to determine the boundary conditions for the viscous adjoint equations and therefore be removed from the cost function. The resulting cost function can be written as

$$\delta I = \int_{B_{IEF}} \left[-n_i \delta S_{ij} \Psi^T f_j + \delta C_g \right] dB + \int_{B_W} \left[n_i \delta S_{ij} \psi_k (\sigma_{jk} - p \delta_{jk}) + \delta C_g \right] dB + \delta I_g \quad (10)$$

The adjoint program has been integrated with a code called ParCAE which is a multi-block parallel flow solver.² Similar properties of the adjoint equations allow them to be solved using the same numerical method as used for the flow equations. All equations are discretized in space with a structured hexahedral grid using a cell-centered finite-volume method. Each grid block is considered as a single entity with only the flow and adjoint quantities exchanged at the block boundaries. The governing equations are solved explicitly in a coupled manner using a five-stage Runge-Kutta scheme toward a steady-state solution with local-time stepping, residual smoothing, and multigrid techniques for convergence acceleration. The computational grid is depicted in Fig. 4 and consisted of 1.6 million grid points. Additional details about the numerical method can be found in Ref. 9.

C. Aerodynamic Evaluation

The vanes are subjected to a favorable external pressure gradient (accelerating freestream), rendering the formal definition for the pressure coefficient problematic due to the lack of a fixed freestream reference condition. In the following discussion, the pressure coefficient is defined as

$$C_p = \frac{P - P_{LE}}{q_{LE}} \quad (11)$$

where the reference quantities p_{LE} and q_{LE} are the area-averaged static and dynamic pressures in the plane of the leading edge of the vane, in the absence of the vane. The specific thrust is defined as

$$T_s = \frac{T}{\dot{m}} \quad (12)$$

Since any mass-flow losses caused by the deflectors can be accounted for with a slight enlargement of the fan exit area, the specific-thrust loss is used to evaluate the performance penalty:

$$\Delta T_s = T_s - T_{s, clean} \quad (13)$$

where the subscript ‘‘clean’’ refers to the nozzle without vanes.

The optimization is performed for a single pair of vanes mounted at an azimuthal angle of $\phi_1 = 90^\circ$. The vane trailing edge is situated at 2 mm (1.1 fan exit heights) upstream of the fan nozzle exit. A NACA0012 airfoil is used as an initial shape. The flow conditions correspond to the fan exit conditions of Table 1. Figure 5(a) shows the surface pressure distribution for a 4-mm chord length vane with a NACA0012 shape at several angles of attack. The line labeled C_p^* denotes the critical pressure coefficient above which the flow is supersonic. With increasing angle of attack, a sharp suction peak develops at the vane leading edge followed by a strong pressure rise acting to thicken the boundary layer. At a high enough angle of attack, the suction peak at the leading edge can cause a supersonic pocket with the possible occurrence of a shock wave. Figure 5(b) plots the corresponding specific-thrust loss versus plume deflection angle. Losses are insignificant at low deflection angles but increase rapidly above a deflection angle of $\varepsilon = 1.0^\circ$. Experiments have shown that deflection angles around $\varepsilon = 1.4^\circ$ are sufficient to produce moderate noise reduction. This corresponds to an angle of attack of $\alpha = 10.0^\circ$ and represents a mild and balanced choice as a design point for shape optimization. This will be referred to as Design Point A. A more aggressive design point with $c = 5$ mm and $\alpha = 12.0^\circ$ has also been considered and will be referred to as Design Point B.

D. Results and Discussion

The optimization summary for Design Point A ($c = 4$ mm and $\alpha = 10.0^\circ$) is shown in Fig. 6. Comparison of the shape in Fig. 6(a) shows that optimization results in a considerably thicker vane ($t/c \approx 0.16$) with a larger leading edge radius. The rounder leading edge helps maintain a favorable pressure gradient over the upper surface of the vane, reducing the thickness of the boundary layer. Comparison of the pressure distributions in Fig. 6(b) shows that the design vane has a nearly constant pressure over the majority of the upper surface with the suction peak at the

leading edge completely removed. The reduction in the adverse pressure gradient compared to the NACA0012 mitigates the possibility of a shock wave developing at higher angles of attack. The Mach number contours in Fig. 6(c) show that, similar to the pressure distribution, the Mach number on the upper surface of the design vane remains nearly constant. A magnified view of Mach number contours near the leading edge of the vane in Fig. 6(d) shows nearly a 25% reduction in the leading edge Mach number reflecting the removal of the suction peak. The optimization results in a reduction of specific-thrust loss from 0.163% to 0.152% (6.8% improvement). This suggests that skin-friction losses resulting from the larger wetted area of the thicker design vane are shadowed by the benefit of a more benign pressure distribution.

The corresponding optimization summary for Design Point B ($c = 5$ mm and $\alpha = 12.0^\circ$) is shown in Fig. 7. The vane extends further upstream into the low Mach and low dynamic pressure region of the nozzle, resulting in a weaker suction peak at the leading edge for the 5-mm NACA0012 case compared to its 4-mm equivalent. The weaker suction at the leading edge alleviates the potential for a supersonic pocket and induced separation at higher angles of attack, suggesting the longer vane yields better overall performance. Similar to the 4 mm case the optimization leads to a thicker vane ($t/c \approx 0.18$) with a larger leading edge radius. The pressure distribution along the upper surface of the design vane is flattened and the leading edge suction peak is removed. The optimization results in a design vane with a specific-thrust loss of 0.271%, which is a 3.0% improvement over the NACA0012 vane.

Though the optimizations are performed at fixed angles of attack ($\alpha = 10.0^\circ$ for Design Vane A and $\alpha = 12.0^\circ$ for Design Vane B), it is important to assess the performance of the design vanes with varying angle of attack. For each design vane, the deflection angle and specific-thrust loss were computed for $0.0^\circ < \alpha < 15.0^\circ$. Figure 8 plots the specific-thrust loss versus deflection angle ε and angle of attack α for Design Vane A. It is clear that the design vanes consistently yield better performance than the NACA0012 vanes. At a deflection angle of $\varepsilon = 2.0^\circ$, the optimization reduces the specific-thrust loss by 11.4%. Figure 9 shows the corresponding plots for Design Point B.

The optimization considers only a two-vane configuration for computational ease. However, noise reduction is typically better when utilizing a four-vane configuration. Considering an arrangement with two pairs of the 4 mm Design Vane A mounted at $\phi_1 = 90^\circ$ and $\phi_2 = 150^\circ$ with $\alpha = 10^\circ$, Fig. 10 compares the pressure distributions of the design vanes and NACA0012 vanes along their midspan. Even though there is some interaction between the upper and lower vane pairs, the nearly constant pressure distribution along the upper surfaces of the vanes are still preserved. This suggests the optimization performed for a single vane pair also applies to the case of two vane pairs, provided that the two pairs are not too close to each other.

III. Acoustic Optimization

A. Acoustic Experiments

The lab-scale nozzles were designed to facilitate in the testing of numerous deflector configurations while minimizing uncertainty due to misalignment of the different nozzle components. This was accomplished by integrating the plug, core nozzle, and aft portion of the fan nozzle into a single base piece connected by fins located well upstream of the nozzle exit. A separate fan nozzle tip was fabricated for each deflector configuration and was securely attached to the base piece, with precise alignment, using the locking arrangement depicted in Figure 11. The attachment surface between the fan nozzle tip and the base portion was equipped with an O-ring to prevent leakage. Figure 12 shows photographs of the base nozzle and fan tips.

The nozzles were fabricated using a rapid-prototyping stereolithography method from a laser cured epoxy resin, with tolerance (layer thickness) of 0.178 mm. A total of 51 nozzle fan tips were generated, corresponding to 50 different 4-vane configurations and one baseline case with no deflectors. Table 2 lists all of the configurations tested with the less aggressive 4 mm Design Vane A (32 total). Table 3 lists the configurations tested with the more aggressive 5mm Design Vane B (18 total). The best combination was also considered with a single porous wedge with a half-angle of $\alpha_w = 20^\circ$ placed on the top of the core nozzle ($\phi_w = 180^\circ$) downstream of the fan nozzle exit at $x_{apex} = 5$ mm. In previous investigations, it has been shown that a porosity of $\beta = 0.5$ provides the best acoustic performance.³ Unlike vane deflectors, the porous wedge has been shown to reduce noise over a large range of polar angles. At a porosity of $\beta = 0.5$, the estimated overall specific thrust loss of the wedge deflector is on the order of 0.5%.¹³ A photograph of the porous wedge is shown in Fig. 13.

The design vanes were manufactured using a photolithography method that utilizes a large digital light projection screen coupled with a series of lenses to layer high accuracy vane cross sections out of UV cured resin. The fabrication accuracy was 0.033 mm. The vane is supported by a thin rectangular base that can be inserted into an identically sized recess on the inner wall of a fan nozzle tip. When inserted, the trailing edge of the vane is

situated at $x_{TE} = -2.0$ mm from the fan nozzle exit. A close-up photograph of Design Vane A manufactured at an angle of attack of $\alpha = 7.5^\circ$ is shown in Fig. 14.

A pressure regulated system delivered metered helium-air mixtures to the primary (core) and secondary bypass (fan) nozzles. The total pressure, p_0 , and mass fraction of helium in each mixture were adjusted to match desired exit velocity and Mach number conditions established in Table 1. This approach has been shown to be an accurate and cost effective method for simulating the acoustic behavior of a full-scale heated jet.¹¹

Noise measurements were performed in the aeroacoustic facility shown in Fig.15. The microphone array consists of twenty four 3.2-mm condenser microphones (Briel & Kjaer, Model 4138). For acoustic surveys, the microphones were arranged with twelve on a downward arm (azimuth angle $\Phi_D = 0^\circ$) and twelve on a sideline arm (azimuth angle $\Phi_{SL} = 60^\circ$). Fig. 15 depicts the configuration of the downward arm; the sideline arm is practically identical. On each arm, the polar angles θ ranged approximately from 20 to 120 deg relative to the jet axis. This arrangement enabled simultaneous measurement of the downward and sideline noise at all the polar angles of interest. The microphones were connected, in groups of four, to six conditioning amplifiers (Briel & Kjaer, Model 2690-A-0S4). The 24 outputs of the amplifiers were sampled simultaneously, at 250 kHz per channel, by three 8-channel multi-function data acquisition boards (National Instruments PCI-6143) installed in a Dell Precision T7400 computer with a Xeon quad-core processor. National Instruments LabView software was used to acquire the signals. The temperature and humidity inside the anechoic chamber were recorded to enable computation of the atmospheric absorption. The microphone signals were conditioned with a high-pass filter set at 300 Hz and a low-pass filter set at 100 kHz. Narrowband spectra were computed using a 4096-point ($\Delta f = 61$ Hz) fast Fourier transform and were corrected for microphone actuator response, free field response and atmospheric absorption. Integration of the corrected spectra yields the overall sound pressure level (OASPL).

The perceived noise level (PNL) and effective perceived noise level (EPNL) are used as the primary metrics for evaluating noise reduction. They are calculated based on engine thrust of 120 kN, flight Mach number of 0.23 and engine angle of attack of 10° . The downward (“flyover”) assessment used an altitude of 2000 ft and climb angle of 4° . The sideline assessment used an altitude of 1500 ft and climb angle of 15° . The PNL calculation procedure is outlined in detail by Papamoschou.¹ The change in EPNL with respect to the baseline configuration is defined so that positive values correspond to noise reduction ($\Delta\text{EPNL} = \text{EPNL}_{\text{Base}} - \text{EPNL}$).

B. Results and Discussion

The acoustic summary for a typical 4-vane configuration is shown in Fig.16. The vane configuration used consists of Design Vane A at $\alpha = 7.5^\circ$, $\phi_1 = 80^\circ$ and $\phi_2 = 120^\circ$. This summary includes narrowband lossless spectra scaled to full-scale frequency (scale factor of 50) at select polar angles. Also included are the directivity of OASPL as well as the PNL versus time and jet polar angle during a flyover. The deflected case, shown in blue, is compared to a baseline configuration with no deflectors, shown in red. First consider the acoustic summary in the downward ($\Phi_D = 0^\circ$) direction. It is clear the noise reduction occurs at shallow polar angles to the jet axis and over a broad frequency range. The directivity shows there is moderate noise benefit for polar angles $\theta < 50^\circ$ with little to no change for $\theta > 50^\circ$. The trends in the sideline ($\Phi_{SL} = 60^\circ$) direction are similar to those in the downward direction, though the magnitude of noise reduction is slightly lessened. The benefit amounts to a reduction in effective perceived noise level of $\Delta\text{EPNL} = 1.08$ dB in the downward direction and $\Delta\text{EPNL} = 1.02$ dB in the sideline direction. If the angle of attack of Design Vane A is increased slightly to $\alpha = 10.0^\circ$, the resultant effect is an increase in the magnitude of noise reduction at low polar angles in both the downward and sideline direction, as seen in the acoustic summary shown in Fig. 17. With the increased flow deflection, a minor noise penalty begins to develop at $\theta > 60^\circ$ due to increased TKE on the upper side of the jet. The noise benefit still significantly outweighs the noise penalty for this configuration yielding $\Delta\text{EPNL} = 2.32$ dB in the downward direction and $\Delta\text{EPNL} = 1.56$ dB in the sideline direction.

The corresponding acoustic summary using the more aggressive Design Vane B at $\alpha = 12.0^\circ$, $\phi_1 = 80^\circ$ and $\phi_2 = 120^\circ$ is depicted in Fig.18. The noise improvements continue with excellent reductions for $\theta < 60^\circ$. There is a 4.8 dB reduction in peak OASPL in the downward direction with a 3.8 dB reduction in the sideline direction. This correlates to an EPNL reduction of $\Delta\text{EPNL} = 2.81$ dB and $\Delta\text{EPNL} = 2.45$ dB, respectively. If the angle of attack is increased to $\alpha = 14.0^\circ$, the trend is broken. Figure 19 shows the noise reduction continues to improve in the downward direction with $\Delta\text{EPNL} = 3.05$ dB, but at the expense of the sideline noise reduction ($\Delta\text{EPNL} = 1.33$ dB). The aggressive deflection also causes a substantial penalty at higher polar angles. This penalty is clearly reflected in the PNL plots versus time and jet polar angle.

For a broad perspective of the noise reduction versus vane azimuthal configuration, the contours in Fig. 20 show ΔEPNL plotted against the vane pair azimuth angles ϕ_1 and ϕ_2 for the case of Design Vane A at angle of attack $\alpha = 7.5^\circ$. Clearly, both pairs of vanes influence noise reduction in the downward direction, Φ_D , evident by the diagonal

gradient present. The results suggest that best downward noise reduction is obtained with lower values of ϕ_1 and ϕ_2 . It is difficult to distinguish a clear trend in the sideline reductions though they appear to be rather insensitive to the upper vane pair angle, ϕ_2 . Unlike in the downward direction, better sideline noise reduction is achieved with higher values of ϕ_1 . The cumulative downward and sideline reductions are also shown. Analogous results are shown in Fig. 21 when the angle of attack of Design Vane A is increased to $\alpha = 10.0^\circ$. This results in minor improvement in the noise reduction observed in both downward and sideline directions but the trends remain similar.

The trends become clear when considering more aggressive deflector vanes. Figure 22 shows Δ EPNL contours for the case of Design Vane B at $\alpha = 12.0^\circ$. The trend in the downward direction remains the same (lower ϕ_1 and ϕ_2 yield better reductions), but a contrasting trend begins to develop in the sideline direction. Higher values of ϕ_1 and ϕ_2 result in better noise reduction. The overall reductions in both observation directions improve significantly over the mild deflector configurations with the best cumulative reduction of 5.26 dB occurring when the lower vane pair is at $\phi_1 = 80^\circ$ and the upper vane pair at $\phi_2 = 120^\circ$. At an angle of attack of $\alpha = 14.0^\circ$, Design Vane B becomes too aggressive, evident by the increased negative correlation between downward and sideline trends evident in Fig. 23. The net effect is a reduction in the cumulative EPNL change, with the best case still occurring at $\phi_1 = 80^\circ$ and $\phi_2 = 120^\circ$.

Figure 24 shows the noise summary for the best 4-vane configuration (Design Vane B, $\alpha = 12.0^\circ$, $\phi_1 = 80^\circ$, $\phi_2 = 120^\circ$) combined with the porous wedge. Inclusion of the wedge reduces noise levels at all polar angles in both the downward and sideline directions. This effect results in very significant noise reductions at lower polar angles and a complete removal of the noise penalty at higher polar angles. This correlates to EPNL reductions of 5.01 dB in the downward direction and 3.89 dB in the sideline direction. The cumulative EPNL reduction is increased by nearly 70% compared to the 4-vane configuration without the wedge.

IV. Concluding Remarks

This study combined aerodynamic and acoustic optimizations toward efficient implementation of fan flow deflection for noise reduction from a nozzle simulating the exhaust of a supersonic turbofan engines. An adjoint method for aerodynamic shape optimization was used to design deflector vanes that provide sufficient flow deflection with minimum thrust penalty. A NACA0012 airfoil was used as an initial shape and two design points were considered yielding a mild deflector (Design Vane A, $c = 4$ mm, $\alpha = 10.0^\circ$) as well as a more aggressive deflector (Design Vane B, $c = 5$ mm, $\alpha = 12.0^\circ$). Optimization leads to a flattened pressure distribution over the upper surface of the vane and the removal of the suction peak at the leading edge. The reduction in the adverse pressure gradient compared to the NACA0012 vane mitigates the possibility of a shock wave forming over the upper surface at higher angles of attack. In addition, the optimal airfoil shape is significantly thicker, which could be beneficial for structural reasons.

The optimal vane airfoil was then used in a parametric acoustic study of 50 deflector configurations with variable vane chord length, angle of attack and azimuth angle. Positioning both deflector pairs at lower azimuthal angles will generally increase downward flow deflection. Too much downward deflection will reduce noise in the downward direction only at the expense of the sideline reduction, and can lead to excessive noise penalty at higher polar angles due to increased turbulent kinetic energy (TKE) levels in the plume. The best configuration utilized Design Vane B deflectors at $\alpha = 12.0^\circ$ with the lower vane pair situated at $\phi_1 = 80^\circ$ and upper vane pair at $\phi_2 = 120^\circ$. This configuration yielded a reduction in EPNL of Δ EPNL = 2.81 dB in the downward direction and Δ EPNL = 2.45 dB in the sideline direction.

The addition of a porous wedge-shaped deflector was also considered. A wedge with 50% porosity and a half-angle of $\alpha_w = 20.0^\circ$ was combined with the best 4-vane configuration. The EPNL was reduced by Δ EPNL = 5.0 dB in the downward direction and Δ EPNL = 3.9 dB in the sideline direction compared to the baseline case. This very significant reduction indicates that the effect of the wedge can be additive to an optimized vane configuration. In practice, the porous wedge would be integrated into the engine pylon (or similar surface) in the form of flaps.³ During noise-sensitive segments of the flight, the flaps could be deployed and the vane deflectors actuated. Computational predictions of specific-thrust loss for the entire engine (including the core stream) are 0.39% from the optimal vane arrangement and 0.53% from the wedge,¹⁰ for a total thrust loss of 0.92%. During portions of the flight when noise reduction is unnecessary, such as cruise, the wedge flaps could be retracted and the vanes positioned at $\alpha = 0^\circ$. Based on our computations, the thrust loss caused by the vanes at zero incidence is 0.04%. Using skin friction data for perforated surfaces¹² with porosity of 40% we estimate that the thrust loss due to the folded wedge flaps is 0.07%. Thus the thrust loss for non-noise-sensitive segments of flight is estimated at 0.11%.

The optimization study performed here underscores the sensitivity of the fan flow deflection method to the deflector parameters and the need for careful design in the practical implementation of this noise reduction approach. For example, differences of 1-2 degrees in the vane angle of attack impact the cumulative EPNL reduction

levels by as much as 2 dB. The advanced manufacturing methods in this study enabled high precision in the deflector parameters and hence robust guidance in the deflector optimization. It is notable that the cumulative noise reduction levels are about 2 dB better than in previous studies with the same nozzle. In addition, we have developed reliable estimates of thrust loss through extensive and detailed computations of the deflector flow fields.

Acknowledgment

The support by NASA Cooperative Agreement NNX07AC62A (monitored by Dr. K.B.M.Q. Zaman) is gratefully acknowledged.

References

1. Papamoschou, D., “Fan Flow Deflection in Simulated Turbofan Exhaust,” *AIAA Journal*, Vol. 44, No. 12, 2006, pp. 3088-3097.
2. Xiong, J., Nielsen, P.E., Liu, F. and Papamoschou, D., “Computation of High-Speed Coaxial Jets with Fan Flow Deflection,” *AIAA Journal*, Vol. 48, No. 10, 2010, pp. 2249-2262.
3. Papamoschou, D., “Pylon Based Jet Noise Suppressors,” *AIAA Journal*, Vol. 47, No. 6, 2009, pp. 1408-1420.
4. Nielsen, P. and Papamoschou, D., “Optimization of Fan Flow Deflection for Supersonic Turbofan Engines,” AIAA Paper 2008-3061, May 2008.
5. Xiong, J., Liu, F. and Papamoschou, D., “Computation of the Flow of a Dual-Stream Jet with Fan Flow Deflectors for Noise Reduction,” AIAA-2009-3254, June 2009.
6. Papamoschou, D., “Engine Cycle and Exhaust Configurations for Quiet Supersonic Propulsion,” *Journal of Propulsion and Power*, Vol. 20, No. 2, 2004, pp. 255-262.
7. Jameson, A., “Aerodynamic Design via Control Theory,” *Journal of Scientific Computing*, Vol. 3, No. 3, 1988, pp. 233-260.
8. Jameson, A., Pierce, N. and Martinelli, L., “Optimum Aerodynamic Design Using the Navier Stokes Equations,” *Theoretical and Computational Fluid Dynamics*, Vol. 10, 1998, pp. 213-237.
9. Liu, F. and Zheng, X., “A Strongly Coupled Time-Marching Method for Solving the Navier-Stokes and $k-\omega$ Turbulence Model Equations with Multigrid,” *Journal of Computational Physics*, Vol. 128, No. 10, 1996, pp. 257-284.
10. Xiong, J., Liu, F. and Papamoschou, D., “Computation of the Flow of a Dual-Stream Jet with External Solid and Perforated Wedge Deflectors for Noise Reduction,” AIAA Paper 2010-4863, June 2010.
11. Papamoschou, D., “Acoustic Simulation of Coaxial Hot Air Jets Using Cold Helium-Air Mixture Jets,” *Journal of Propulsion and Power*, Vol. 23, No. 2, 2007, pp. 375-381.
12. Wolter, J.D., “Drag Measurements of Porous Plate Acoustic Liners,” NASA/TM—2005-213570, March 2005.

Table 1. Cycle conditions for the B27 Nozzle.

Quantity	Primary (Core)	Secondary (Fan)
NPR	2.00	2.25
M	1.03	1.15
U (m/s)	600	400
$A_S/A_P = 1.40$		$U_S/U_P = 0.67$

Table 2. Design Vane A configurations and corresponding reduction in cumulative EPNL.

Design Vane A		ϕ_2 (deg)			
$\alpha = 7.5^\circ$		120	130	140	150
ϕ_1 (deg)	60	2.87 dB	2.04 dB	2.30 dB	1.28 dB
	70	2.59 dB	2.69 dB	2.38 dB	2.21 dB
	80	2.10 dB	2.57 dB	2.34 dB	2.30 dB
	90	2.51 dB	3.07 dB	2.50 dB	3.14 dB

Design Vane A		ϕ_2 (deg)			
$\alpha = 10^\circ$		120	130	140	150
ϕ_1 (deg)	60	3.54 dB	3.73 dB	3.54 dB	2.01 dB
	70	3.53 dB	4.10 dB	3.23 dB	2.34 dB
	80	3.88 dB	3.34 dB	2.50 dB	1.97 dB
	90	3.76 dB	3.06 dB	3.11 dB	3.68 dB

Table 3. Design Vane B configurations and corresponding reduction in cumulative EPNL.

Design Vane B		ϕ_2 (deg)		
$\alpha = 12^\circ$		110	120	130
ϕ_1 (deg)	70	4.64 dB	4.09 dB	4.68 dB
	80	4.18 dB	5.26 dB	5.05 dB
	90	4.03 dB	4.63 dB	4.56 dB

Design Vane B		ϕ_2 (deg)		
$\alpha = 14^\circ$		110	120	130
ϕ_1 (deg)	70	4.25 dB	4.13 dB	4.07 dB
	80	3.66 dB	4.39 dB	3.85 dB
	90	3.67 dB	4.11 dB	4.56 dB

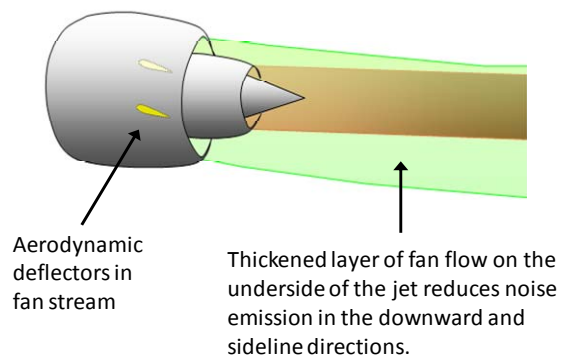


Fig. 1 Illustration of fan flow deflection (FFD).

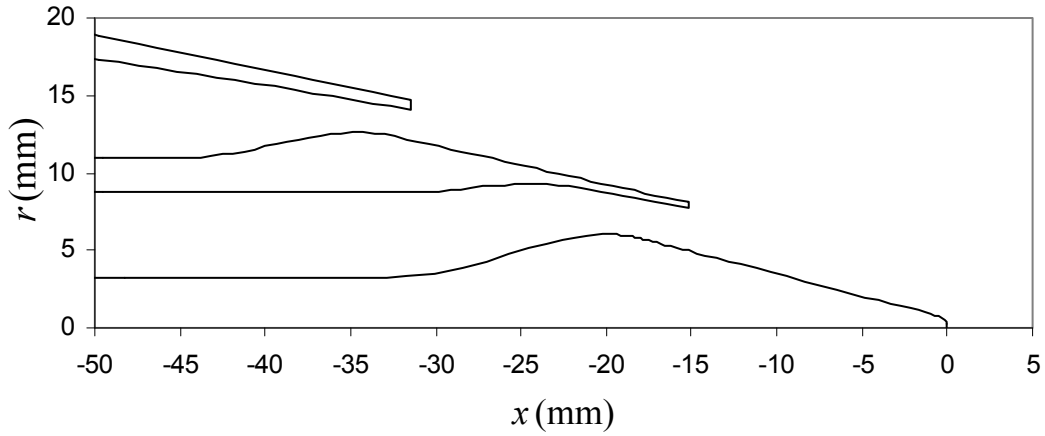


Fig. 2 B27 nozzle coordinates.

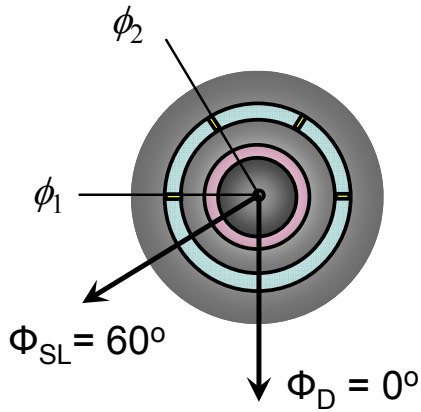


Fig. 3 Definition of azimuth angles.

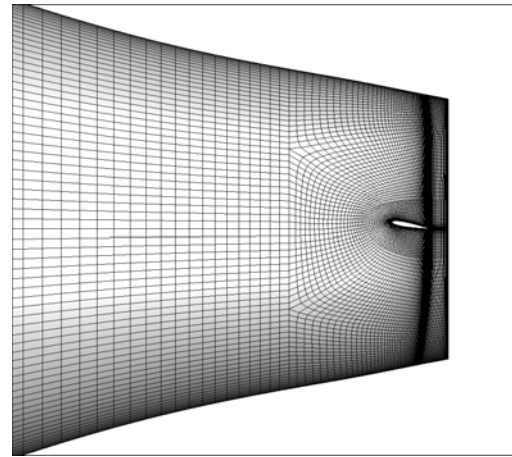


Fig. 4 Computational grid.

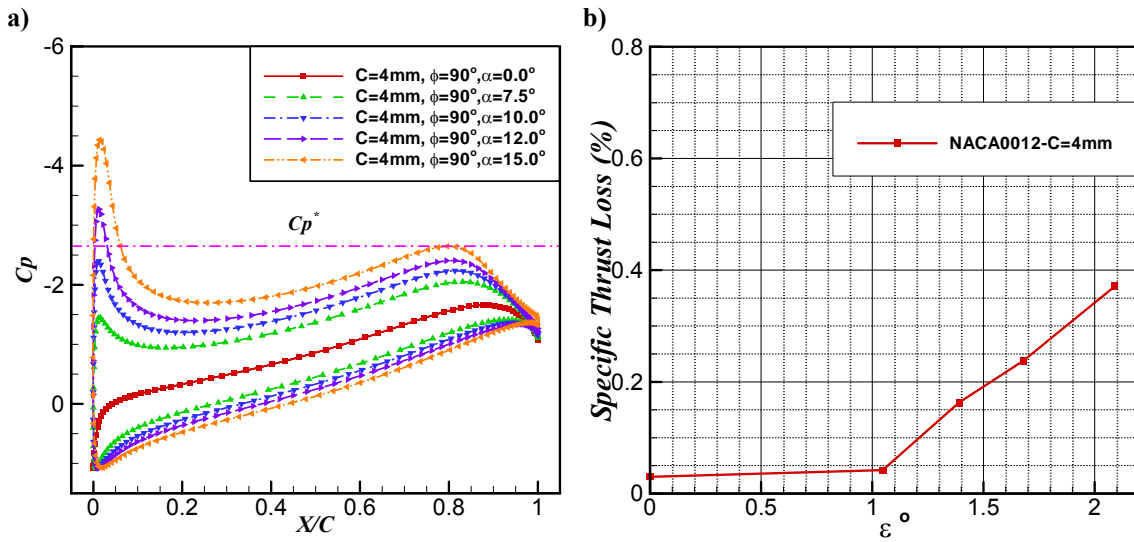


Fig. 5 Performance of 4-mm NACA0012 vanes. a) Pressure distribution versus vane angle of attack; b) percent specific thrust loss versus flow deflection angle.

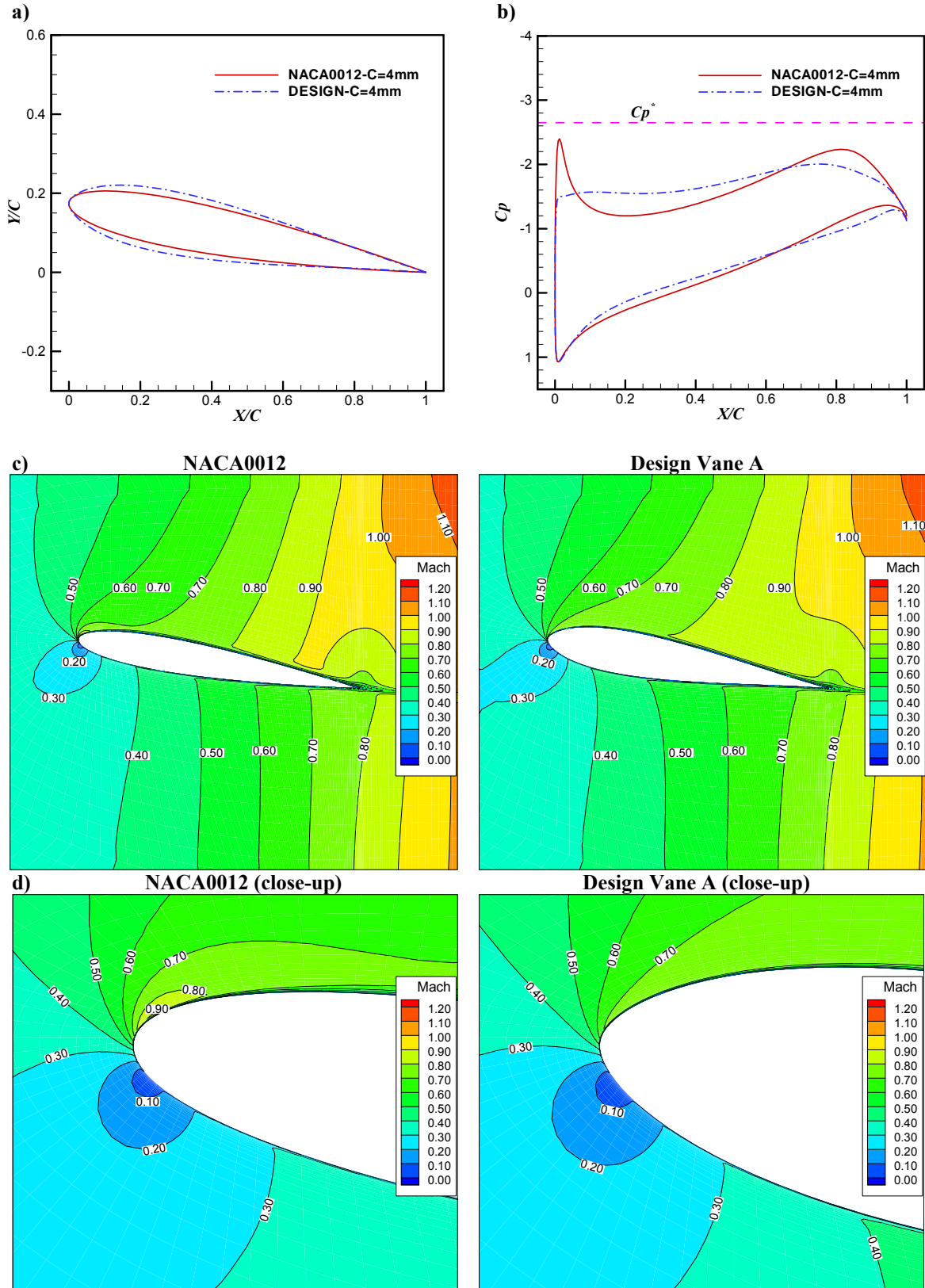


Fig. 6 Optimization summary for Design Point A: a) shape distribution; b) pressure distribution; c) Mach number contours at the midspan; d) leading edge Mach number contours at the midspan.

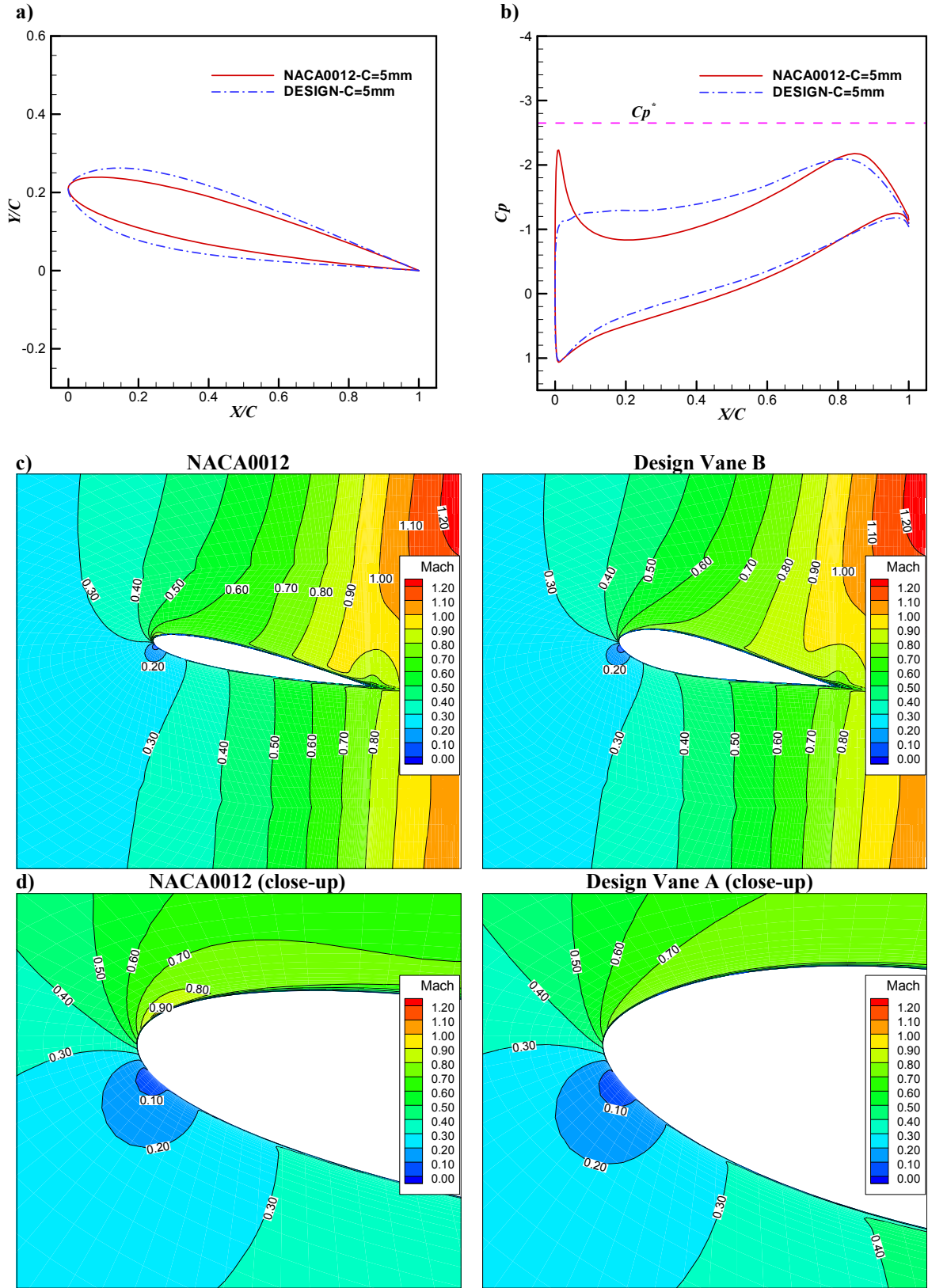


Fig. 7 Optimization summary for Design Point B: a) shape distribution; b) pressure distribution; c) Mach number contours at the midspan; d) leading edge Mach number contours at the midspan.

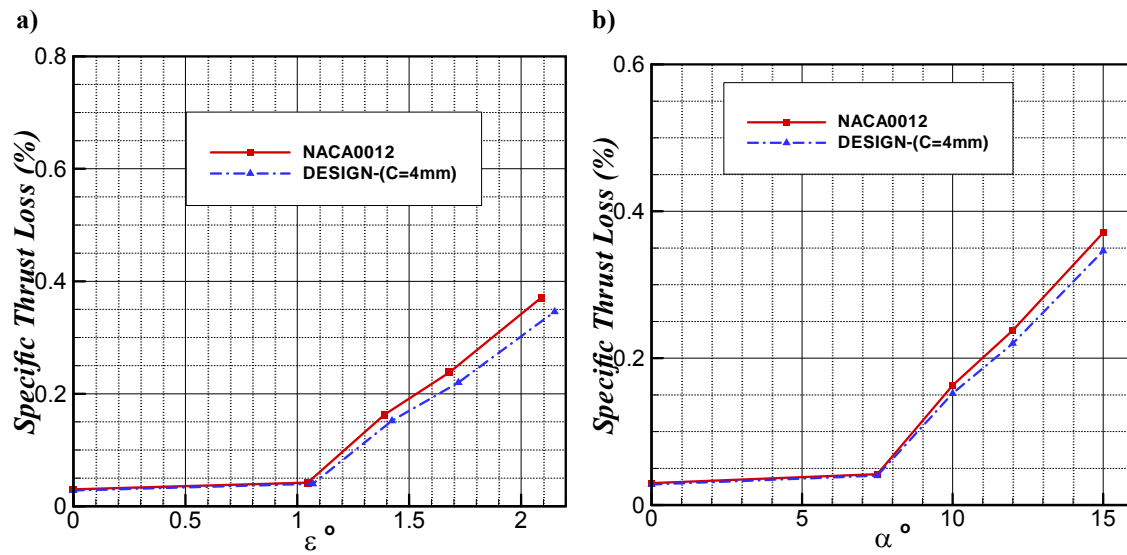


Fig. 8 Percent specific-thrust loss for Design Vane A versus a) flow deflection angle and b) angle of attack.

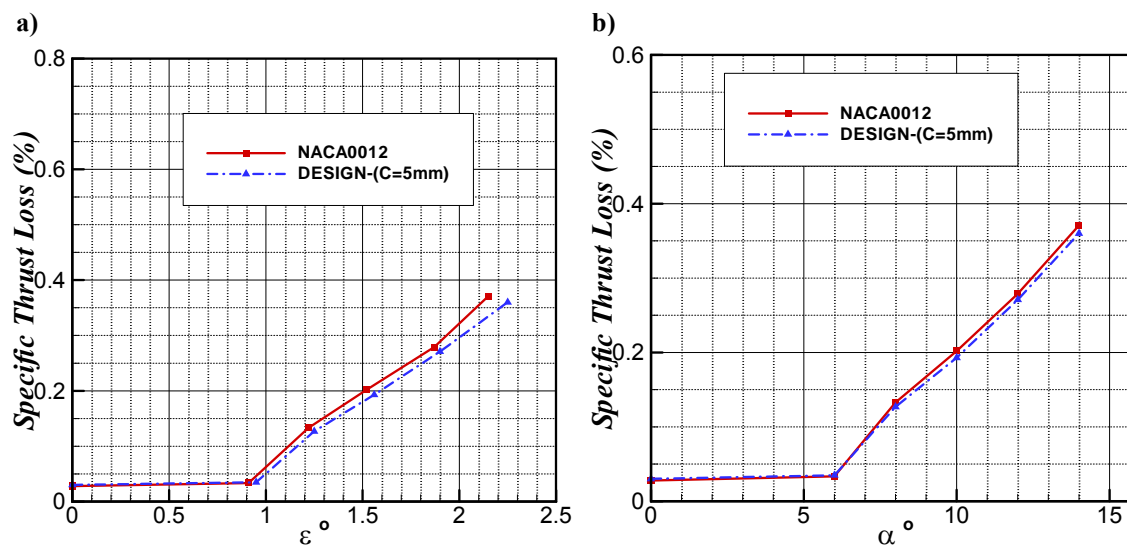


Fig. 9 Percent specific-thrust loss Design Vane B versus a) flow deflection angle and b) angle of attack.

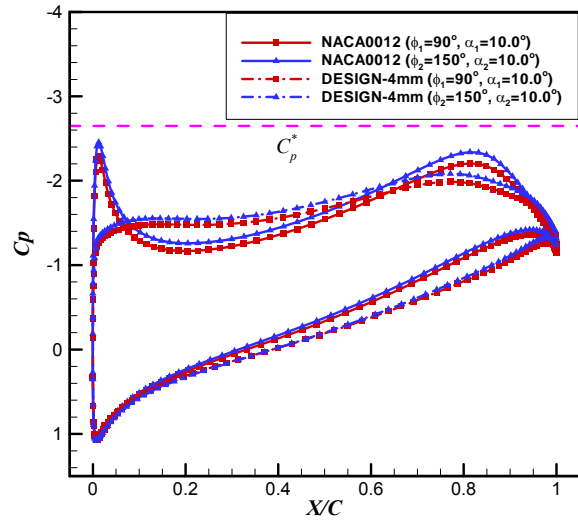


Fig. 10 Pressure distributions at mid-span of airfoil in a 4-vane configuration.

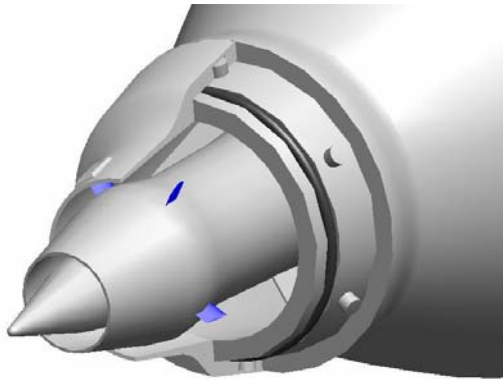


Fig. 11 Details of experimental nozzle arrangement.

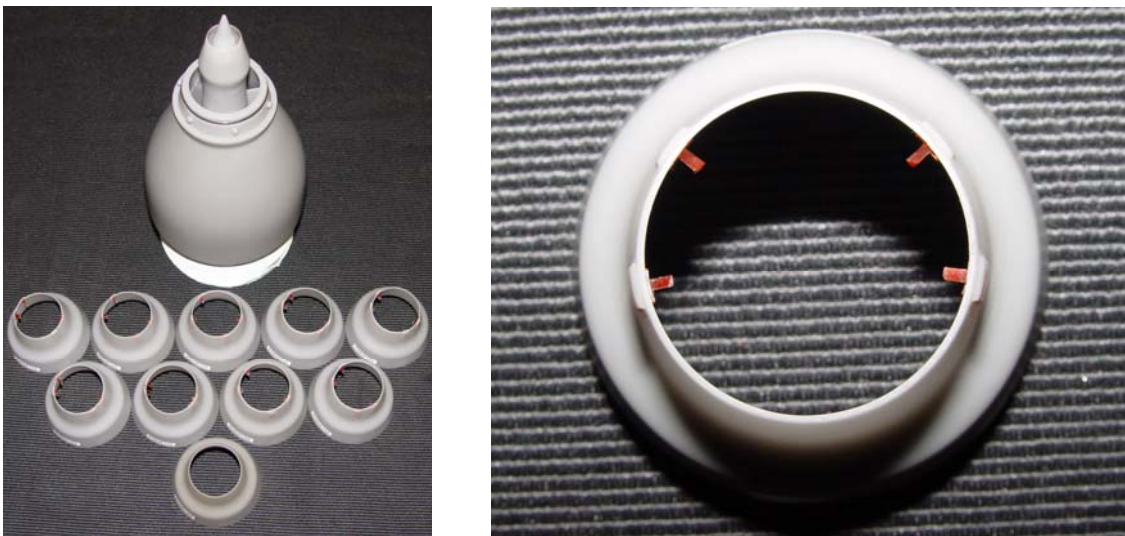


Fig. 12 Photographs of the experimental base nozzle and fan nozzle tips.



Fig. 13 Photograph of porous wedge deflector.

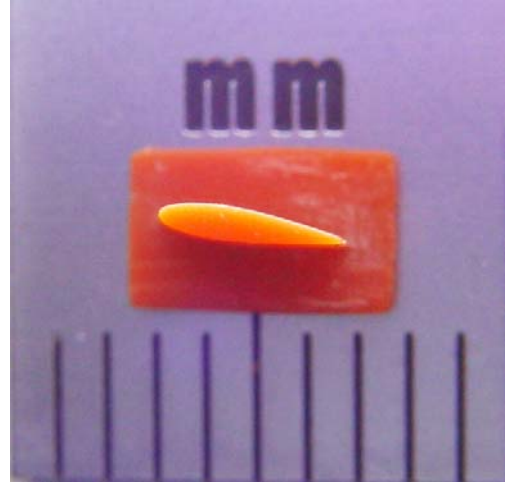


Fig. 14 Close-up photograph of experimental design vanes.

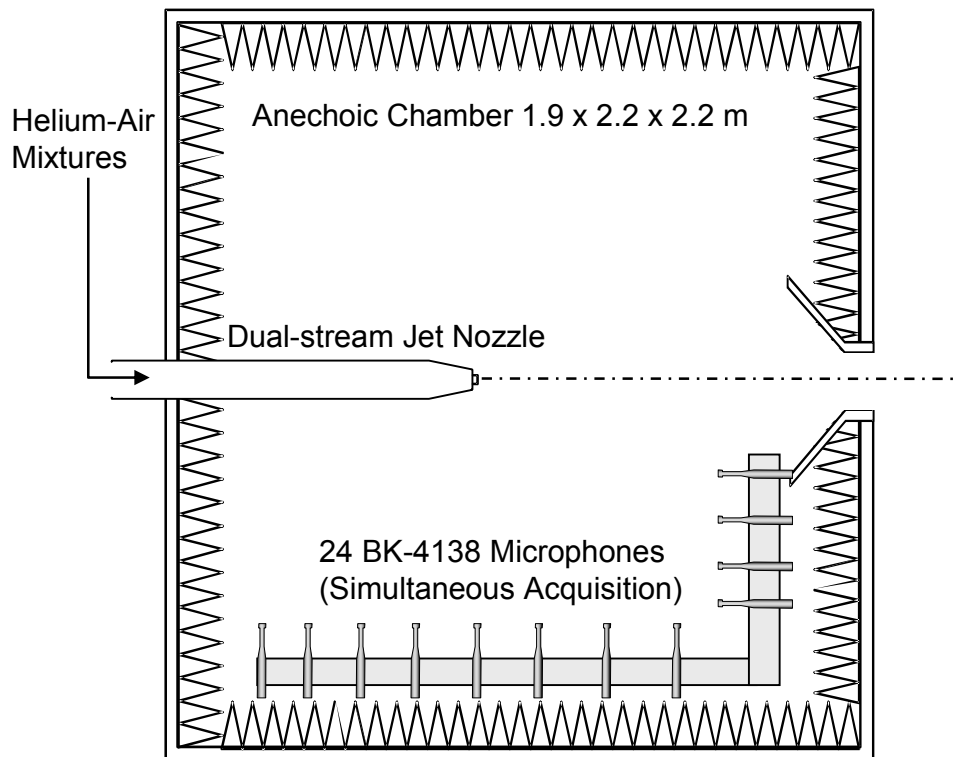


Fig. 15 Anechoic facility and microphone array.

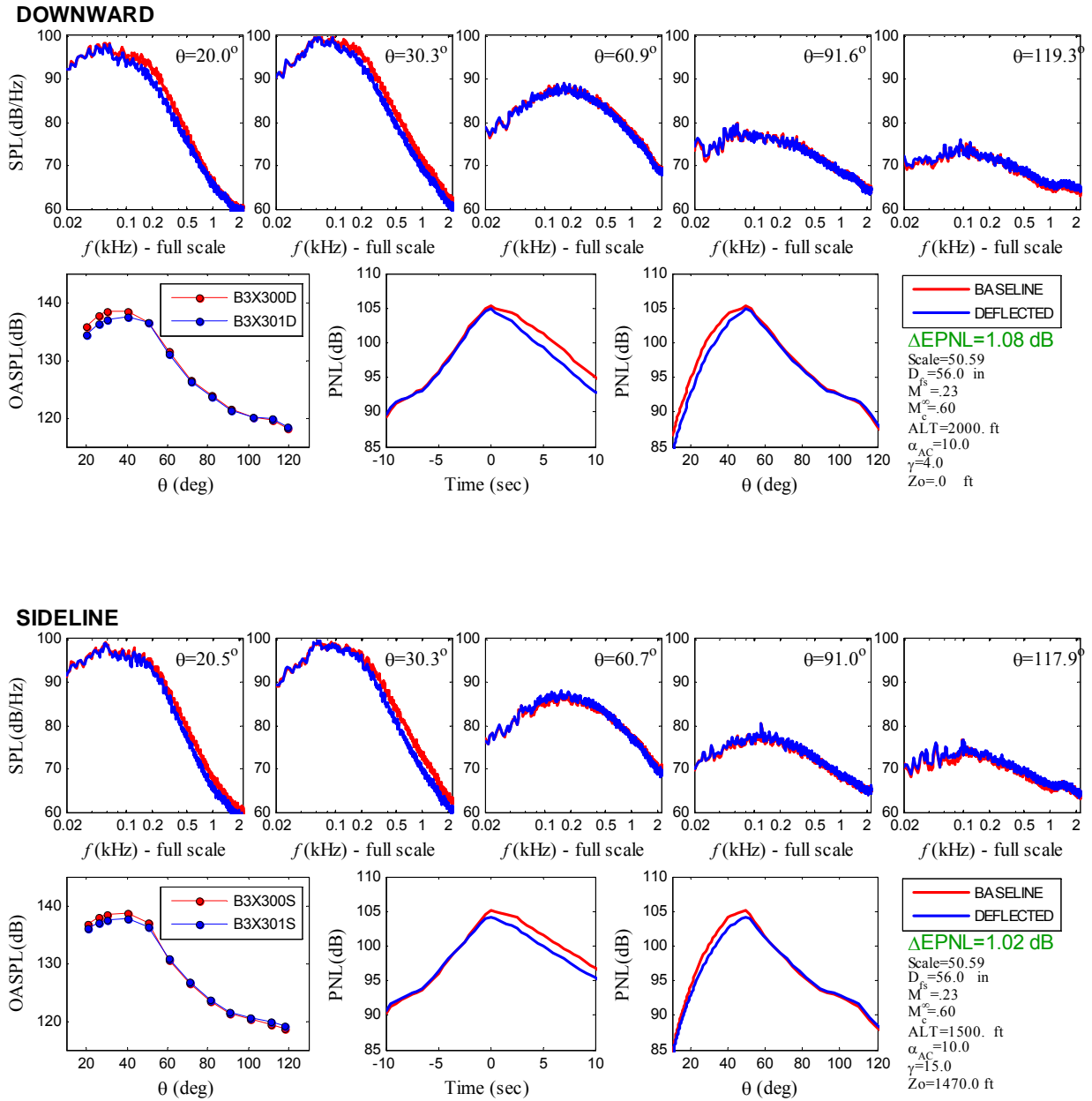


Fig. 16 Acoustic summary for Design Vane A at $\alpha = 7.5^\circ$, $\phi_1 = 80^\circ$, $\phi_2 = 120^\circ$.

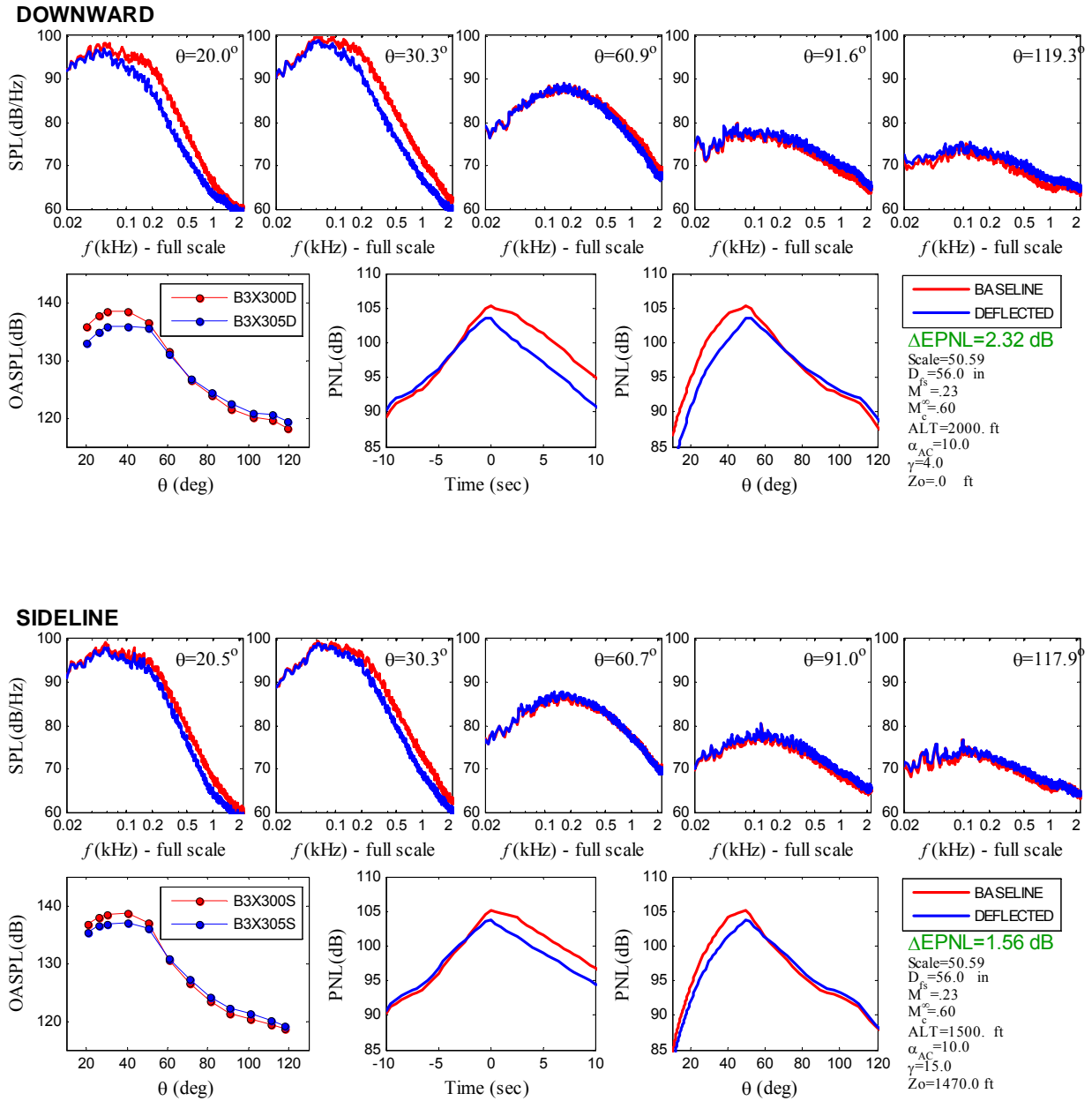


Fig. 17 Acoustic summary for Design Vane A at $\alpha = 10.0^\circ$, $\phi_1 = 80^\circ$, $\phi_2 = 120^\circ$.

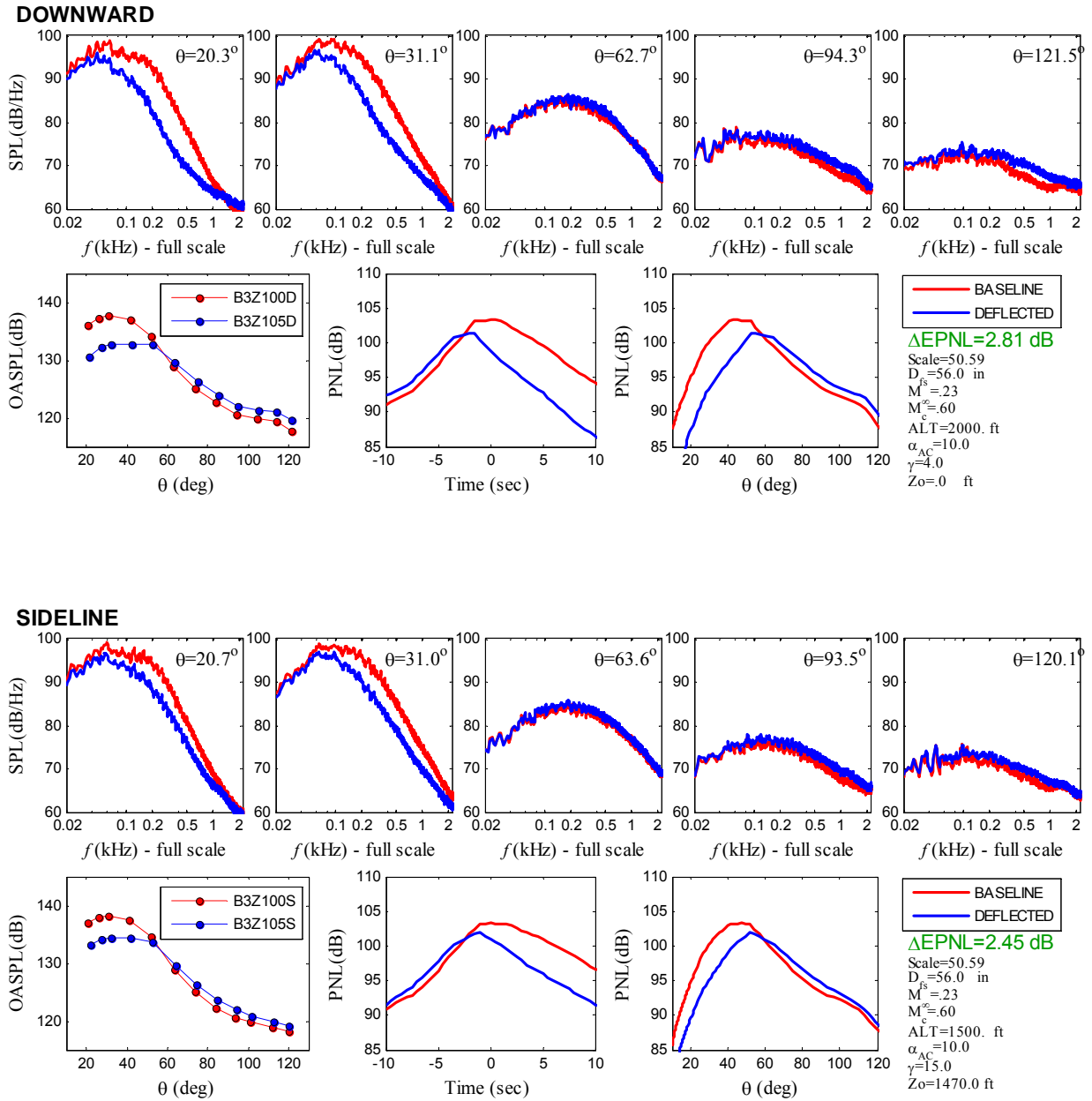


Fig. 18 Acoustic summary for Design Vane B at $\alpha = 12.0^\circ$, $\phi_1 = 80^\circ$, $\phi_2 = 120^\circ$.

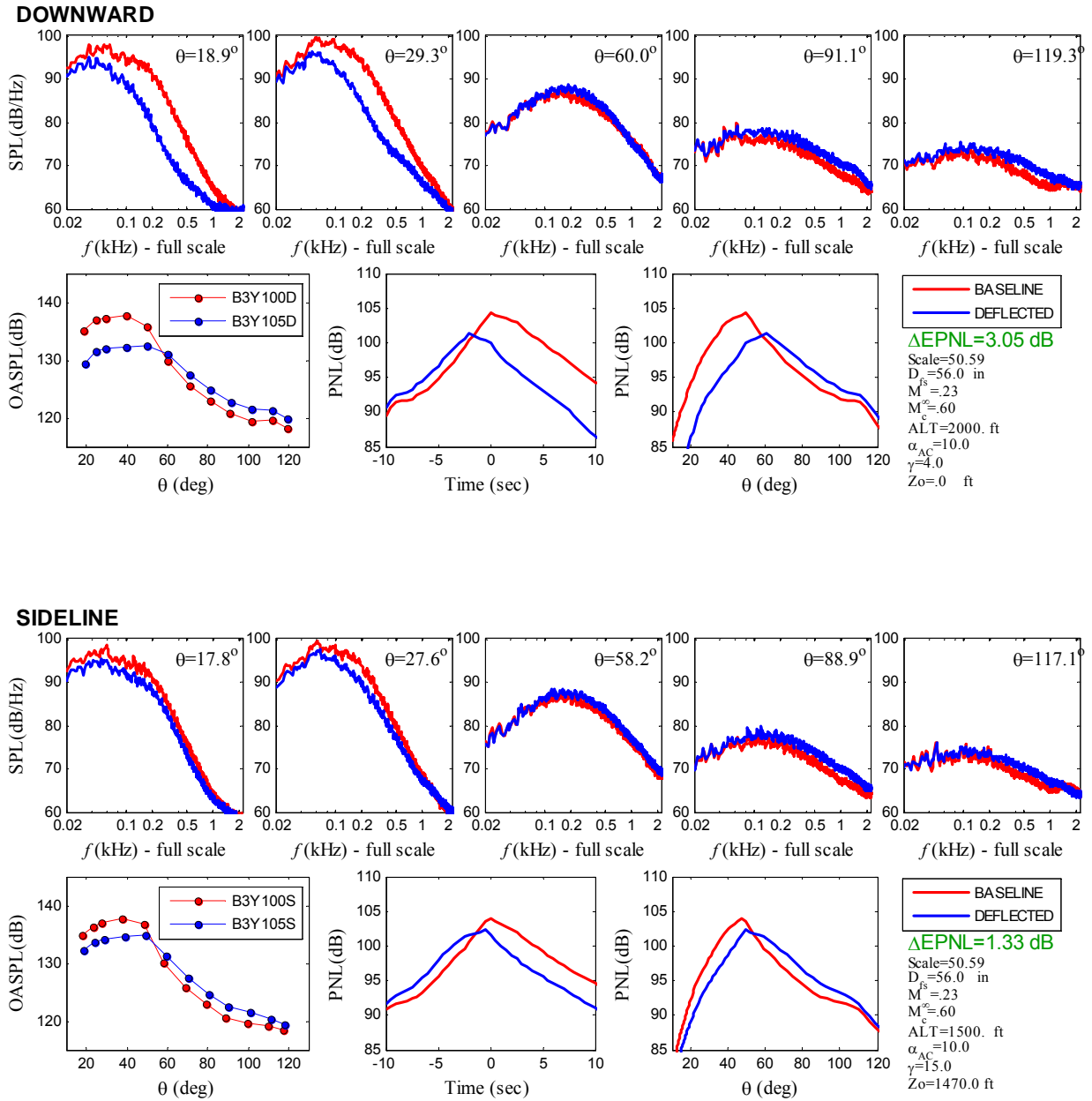


Fig. 19 Acoustic summary for Design Vane B at $\alpha = 14.0^\circ$, $\phi_1 = 80^\circ$, $\phi_2 = 120^\circ$.

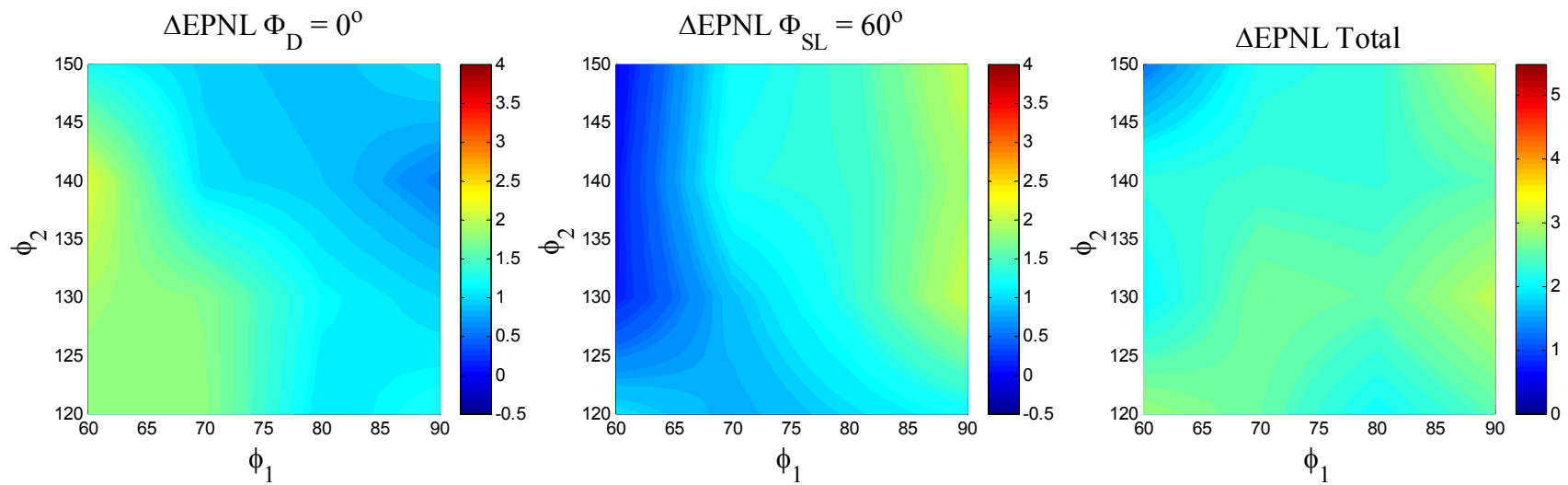


Fig. 20 Contours of noise reduction versus vane azimuthal position for Design Vane A at $\alpha = 7.5^\circ$.

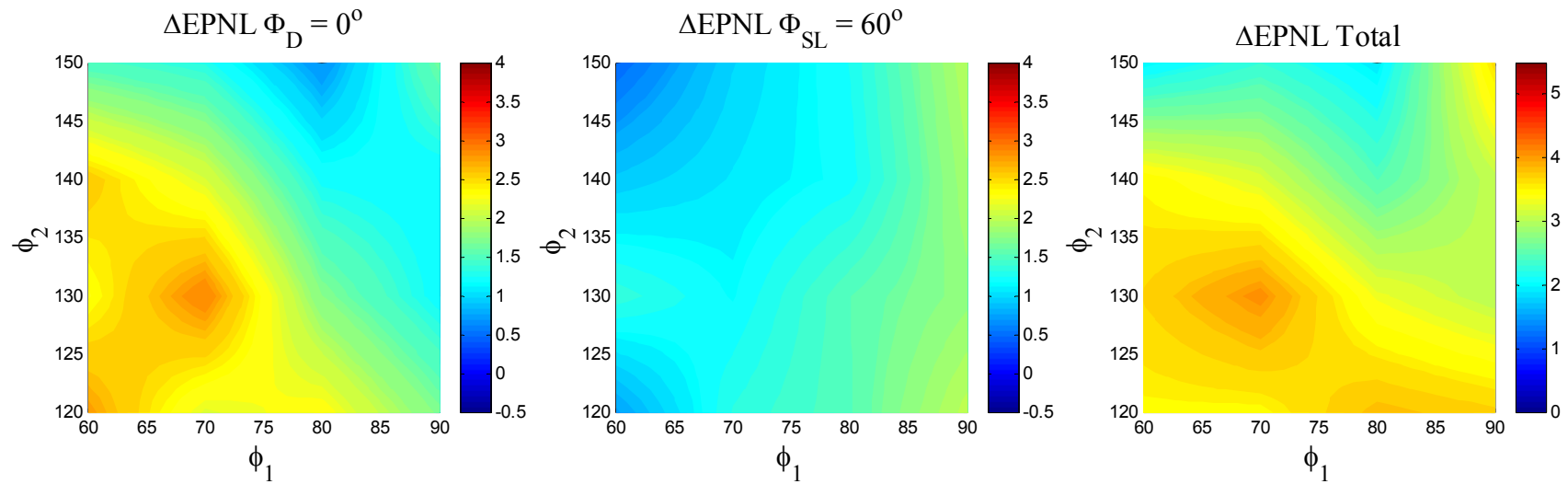


Fig. 21 Contours of noise reduction versus vane azimuthal position for Design Vane A at $\alpha = 10.0^\circ$.

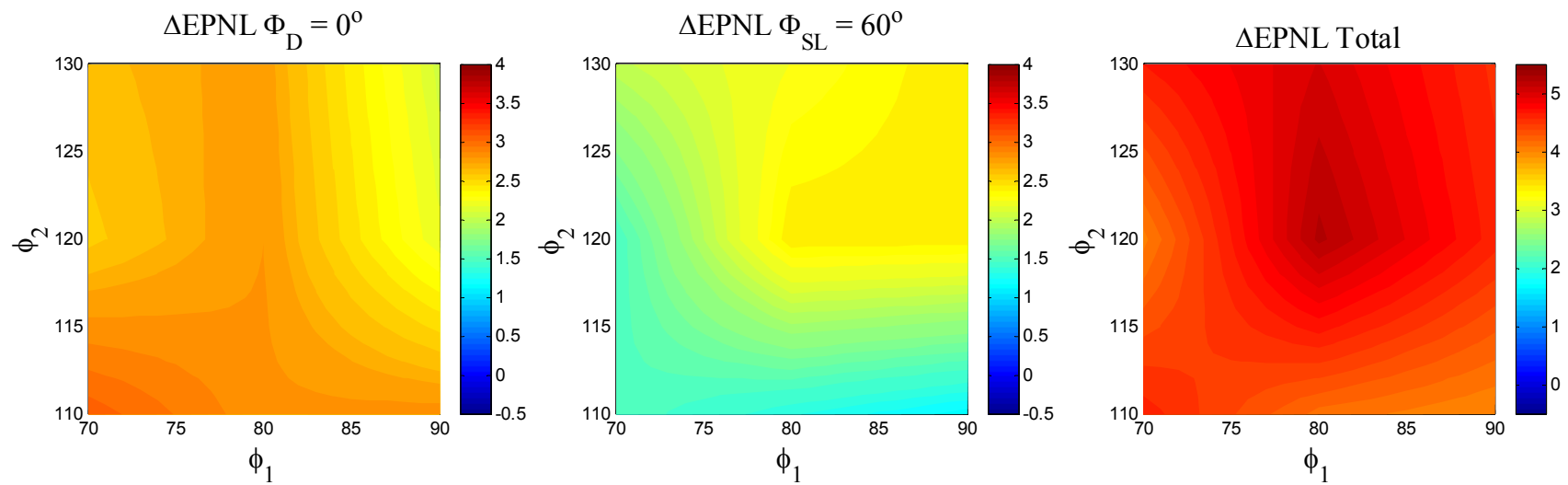


Fig. 22 Contours of noise reduction versus vane azimuthal position for Design Vane B at $\alpha = 12.0^\circ$.

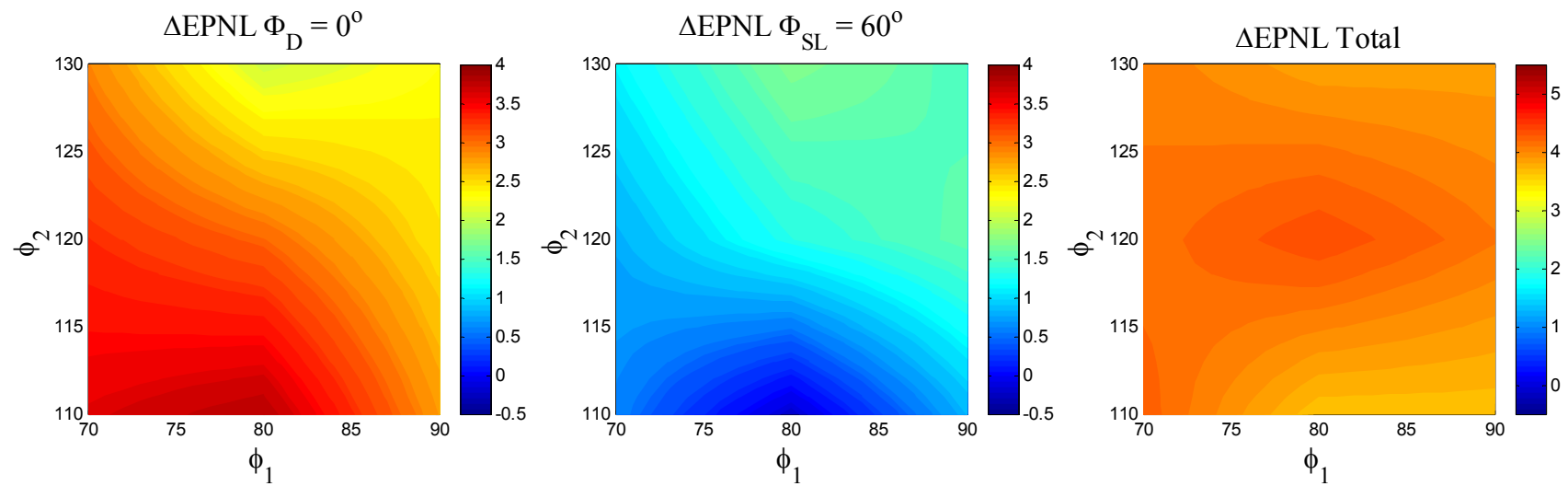


Fig. 23 Contours of noise reduction versus vane azimuthal position for Design Vane B at $\alpha = 14.0^\circ$.

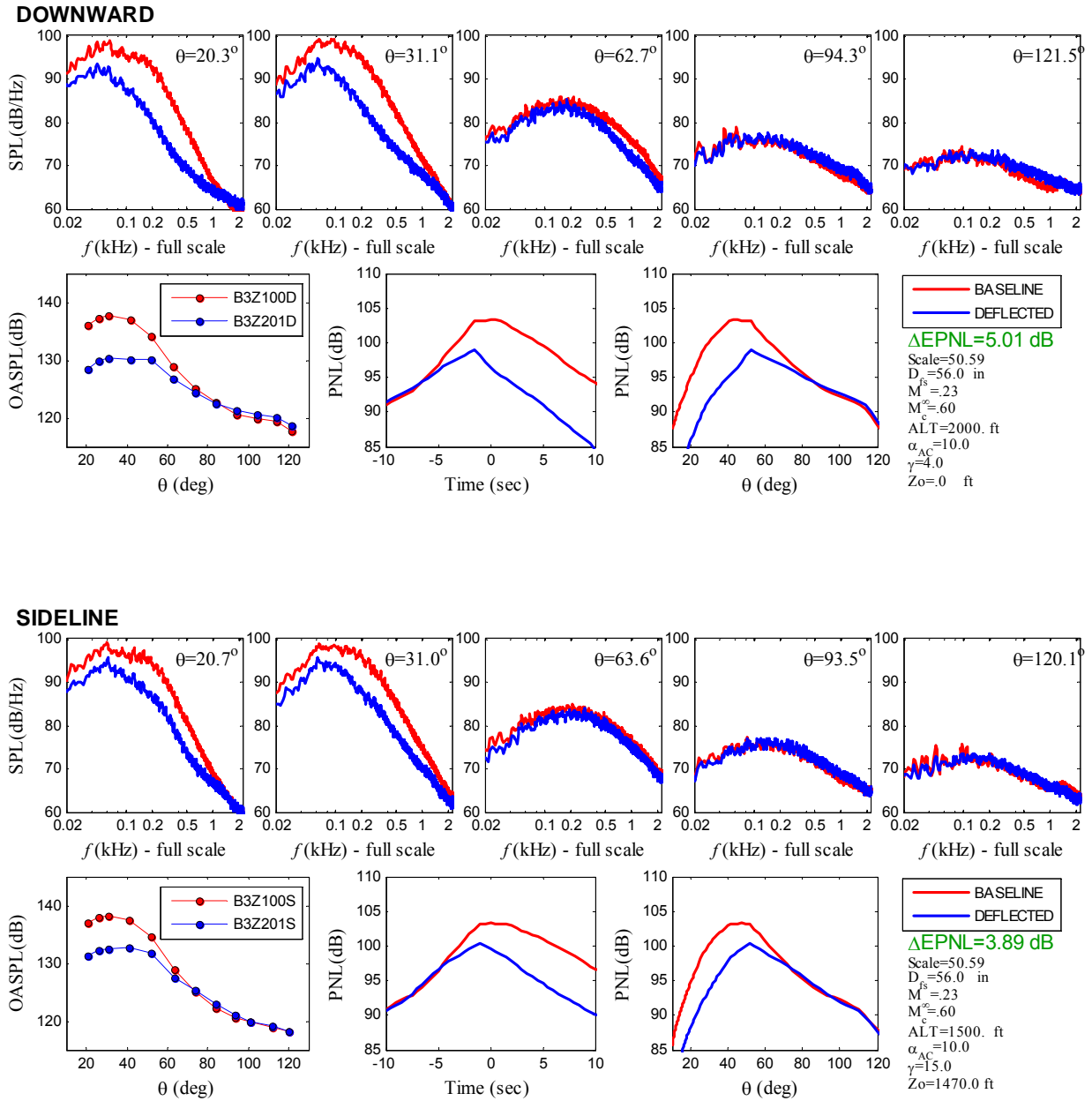


Fig. 24 Acoustic summary for Design Vane B at $\alpha = 12.0^\circ$, $\phi_1 = 80^\circ$, $\phi_2 = 120^\circ$ with porous wedge.